

# Realization of Wigner-Mott insulators in 6R-TaS<sub>2</sub> superconductor

Hongqin Xiao<sup>1,2#</sup>, Geng Li<sup>1,2,3#,\*</sup>, Yuxuan He<sup>1,2#</sup>, Ke Zhu<sup>1,2#</sup>, Yuhan Ye<sup>1,2,3</sup>, Yumeng Li<sup>1,2</sup>, Lijing Huang<sup>1,2</sup>, Haitao Yang<sup>1,2,3</sup>, Ziqiang Wang<sup>4</sup> & Hong-Jun Gao<sup>1,2,3\*</sup>

<sup>1</sup> Beijing National Center for Condensed Matter Physics and Institute of Physics, Chinese Academy of Sciences, Beijing 100190, China

<sup>2</sup> School of Physical Sciences, University of Chinese Academy of Sciences, Beijing 100190, PR China

<sup>3</sup> Hefei National Laboratory, Hefei 230088, China

<sup>4</sup> Department of Physics, Boston College, Chestnut Hill, MA 02467, USA

Wigner-Mott insulating states represent a paradigmatic manifestation of strong electronic correlations, in which long-range Coulomb interactions drive spontaneous charge ordering and enable Mott localization at fractional electronic fillings<sup>1-6</sup>. Such states have been theoretically proposed to arise from the cooperative interplay between onsite and inter-site Coulomb interactions<sup>1,2</sup>. However, experimental realization of a Wigner-Mott insulator has remained elusive. Here we report the observation of a Wigner-Mott insulating states in 6R-TaS<sub>2</sub> using scanning tunneling microscopy. By locally injecting electrons into the depleted 1T layer, we induce distinct Star-of-David charge-ordered superstructures and realize a cascade of insulating phases. In particular, a  $\sqrt{3}\times\sqrt{3}$  superstructure constitutes a Wigner-Mott insulating state, characterized by a robust Mott gap despite fractional filling. Comparative measurements reveal that the conventional  $1\times 1$  Mott state at integer filling is governed predominantly by onsite interaction  $U$ , whereas the  $\sqrt{3}\times\sqrt{3}$  fractional-filling Mott state requires the cooperative effects of both  $U$  and long-range Coulomb interaction  $V$ . Our results provide not only the direct microscopic evidence for a Wigner-Mott mechanism, but also establish a platform for the controllable realization and investigation of Wigner-Mott insulating states.

<sup>#</sup>These authors contributed equally to this work.

\*Correspondence to: hjgao@iphy.ac.cn; gengli.iop@iphy.ac.cn.

The Mott insulating state, in which strong onsite Coulomb repulsion  $U$  prohibits double electron occupancy and forces electrons to localize on individual lattice sites, forms the foundation for a wide range of correlated quantum phases<sup>7</sup>. Doping a Mott insulator away from integer-filling leads to exotic quantum states, such as unconventional superconductivity<sup>8-10</sup>, spin density wave<sup>11,12</sup>, and other exotic collective states<sup>3,13-15</sup>. Beyond this conventional paradigm, it has been theoretically proposed that Mott localization may also emerge at fractional fillings when long-range Coulomb interactions drive spontaneous charge ordering, effectively generating an emergent superlattice with an odd number of electrons per unit cell<sup>1,2</sup>. In this scenario, commonly referred to as a Wigner-Mott insulator, charge ordering driven by nonlocal interactions effectively restores integer filling on the emergent supercell, enabling Mott localization far away from integer filling<sup>1,2</sup>. While fractional-filling insulating states have been extensively explored in moiré superlattices<sup>3-6</sup>, experimental signatures of Wigner-Mott physics have so far remained indirect. In particular, the simultaneous microscopic observation of interaction-driven charge order and genuine Mott localization characterized by well-defined Hubbard bands and a hard Mott gap within the same phase has yet to be achieved.

$6R$ -TaS<sub>2</sub> provides a unique layered platform for investigating strong electronic correlations in reduced dimensions<sup>16-20</sup>. In this van der Waals crystal,  $1T$  and  $1H$  layers of TaS<sub>2</sub> are alternately stacked along the  $c$ -axis, forming electronically distinct layers that are weakly coupled through interlayer charge transfer<sup>21</sup>. This natural heterostructure enables the coexistence and interplay of localized and itinerant electronic states, creating a favorable environment for correlation-driven phenomena. Indeed, a variety of exotic quantum states have been reported in related TaS<sub>2</sub>-based layered systems, including artificial heavy-fermion behavior arising from Kondo coupling in monolayer  $1T/1H$  heterostructures<sup>22</sup>, as well as topological superconductivity in stacked  $1T/1H$  compounds<sup>23,24</sup>. More recently, transport measurements<sup>17</sup> have suggested the presence of a hidden ordered state that breaks time-reversal symmetry in  $6R$ -TaS<sub>2</sub>. The coexistence and competition among these correlated electronic phases highlight  $6R$ -TaS<sub>2</sub> as a promising platform for exploring interaction-driven insulating states, including Mott and Wigner-Mott physics.

In this Letter, we report the real-space visualization of Wigner-Mott insulating states in the layered superconductor  $6R$ -TaS<sub>2</sub>. Using scanning tunneling microscopy and spectroscopy (STM/STS), we locally inject electrons into the  $1T$  layer and controllably tune the electronic filling, thereby generating a cascade of emergent insulating phases. At the microscopic level, we resolve distinct regimes of conventional Mott localization and Wigner-Mott localization, distinguished by the absence or presence of spontaneous charge ordering.

6R-TaS<sub>2</sub> crystallizes in a space group of R3m with a stacking sequence of alternating 1T and 1H layers (Fig. 1a), and lattice parameters  $a_0 = b_0 = 3.3$  Å and  $c_0 = 35.8$  Å (Extended Data Fig. 1). These layers are coupled through vdW force, with each 1T (1H) layer sliding one-third of the lattice constant with respect to the adjacent layer of the same type. Upon cleavage, the surface will reveal either the 1T or 1H configuration (Fig. 1b,c). The crystal undergoes a commensurate CDW transition at  $\sim 303$  K, and exhibits superconductivity at  $T_c \sim 3.3$  K (Extended Data Fig. 1c,d). Below the CDW transition temperature, the 1T layer undergoes a periodic lattice distortion (Fig. 1b), forming a characteristic Star-of-David (SoD) structure (Fig. 1b). Consequently, a  $\sqrt{13} \times \sqrt{13} R13.9^\circ$  CDW pattern emerges (Fig. 1d-f).

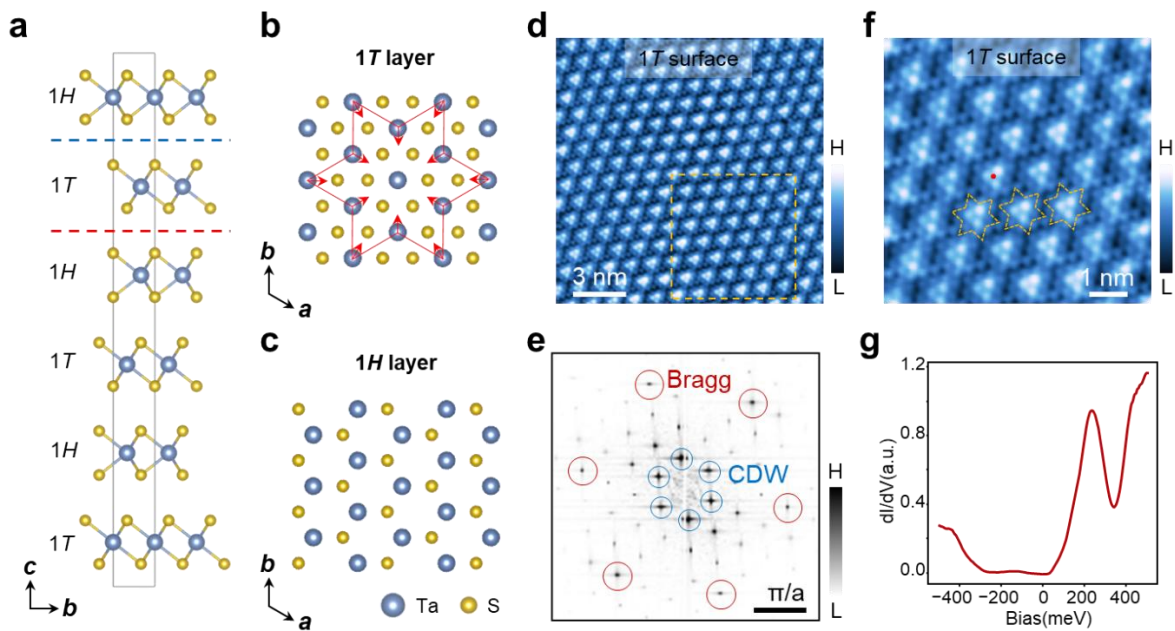


**Fig. 1 | Crystal structure and STM/S of the cleaved surfaces of 6R-TaS<sub>2</sub>.** **a**, Side view of the crystal structure of 6R-TaS<sub>2</sub>, showing stacking of 1T and 1H layers along the  $c$  axis. **b,c**, Top view of the 1T and 1H layers, respectively. **d**, STM image of the 1T surface, showing the  $\sqrt{13} \times \sqrt{13}$  SoD pattern (scanning settings:  $V_s = 500$  mV,  $I_t = 1$  nA). **e**, FT image of **d**, showing clearly the  $\sqrt{13} \times \sqrt{13}$  CDW spots. **f**, Atomically-resolved STM image of the yellow square in **d** (scanning settings:  $V_s = 500$  mV,  $I_t = 1$  nA). **g**,  $dI/dV$  spectrum taken at the center of a SoD (red dot in **f**).

In a pristine 1T layer, each SoD hosts one localized unpaired 5d electron from the center Ta atom, leading to a Mott insulating state. However, in the stacked 1T/1H heterostructure, substantial interlayer

charge transfer depletes the  $1T$  layer of electrons, driving it far away from integer filling while preserving the underlying SoD framework, as have been observed in  $4Hb$ -TaS<sub>2</sub> (Ref. <sup>24,25</sup>) and the  $1T/1H$  monolayer heterostructure<sup>21,22,26-28</sup>. In  $6R$ -TaS<sub>2</sub>, similar charge transfer from the  $1T$  to the  $1H$  layers depletes electrons from the SoDs, resulting in a hole-doped Mott insulating phase, with the lower Hubbard band (LHB) shifted slightly above the Fermi level (Fig. 1g). As a result, the  $1T$  layer in  $6R$ -TaS<sub>2</sub> realizes a highly correlated, low-density electronic system that is qualitatively distinct from both the stoichiometric Mott state of bulk  $1T$ -TaS<sub>2</sub> and a conventionally doped Mott insulator. In this regime, long-range Coulomb interactions are expected to play a dominant role, opening the possibility for electrons to self-organize into emergent charge-ordered superlattices and thereby re-establish Mott localization at fractional fillings described by the Wigner-Mott scenario. In contrast, the  $1H$  layer develops a  $3\times 3$  CDW phase (Fig. 1h,i). At temperatures below  $T_c$ , superconductivity develops exclusively in the  $1H$  layers, with a V-shaped nodal gap<sup>17</sup> of  $\sim 0.46$  meV (Extended Data Fig. 2). This gives  $2\Delta/k_B T_c \sim 3.23$ , revealing a weak coupling superconducting state<sup>24,29</sup>.

We develop a technique to tune the electron filling in the SoDs of the surface  $1T$  layer. The voltage pulses applied via an STM tip can induce a transient current flow, injecting electrons<sup>30</sup> into the  $1T$  layer (Fig. 2a). These injected electrons become trapped in the SoDs, giving rise to a mosaic pattern that appears as clusters of bright SoDs (Fig. 2b,c). Notably, this mosaic pattern emerges only when the applied voltage exceeds 1.2 V, indicating a threshold energy for the electron injection process. With further approaching the tip towards the substrate and performing slow, repeated scans in this region, the electron-injected-SoDs (EI-SoDs) are gradually depleted via tunneling events, ultimately leading to the recovery of the original  $\sqrt{13}\times\sqrt{13}$  CDW (Fig. 2d). As a result, the creation and removing of the EI-SoDs is reversible.

Under high voltage pulses, large-scale mosaic pattern is observed (Fig. 2e). The EI-SoDs could form short-range ordered superstructures<sup>31</sup> due to long-range Coulomb interactions. Depending on the filling level of electrons injected by the STM tip, we observe two distinct ordered superstructures of electron-injected SoD (EI-SoD) clusters: a  $1\times 1$  lattice (Fig. 2f) and a  $\sqrt{3}\times\sqrt{3}$  lattice (Fig. 2g). In the  $1\times 1$  phase, each EI-SoD hosts a single injected electron, corresponding to an integer filling of one electron per SoD. By contrast, the  $\sqrt{3}\times\sqrt{3}$  superstructure corresponds to a fractional filling of one electron per three SoDs (Extended Data Fig. 3). These ordered domains typically extend over lateral length scales of approximately 20-30 nm. Corresponding FT image shows clearly the coexistence of the  $\sqrt{3}\times\sqrt{3}$  superstructure and the  $\sqrt{13}\times\sqrt{13}$  CDW (Fig. 2g,h).

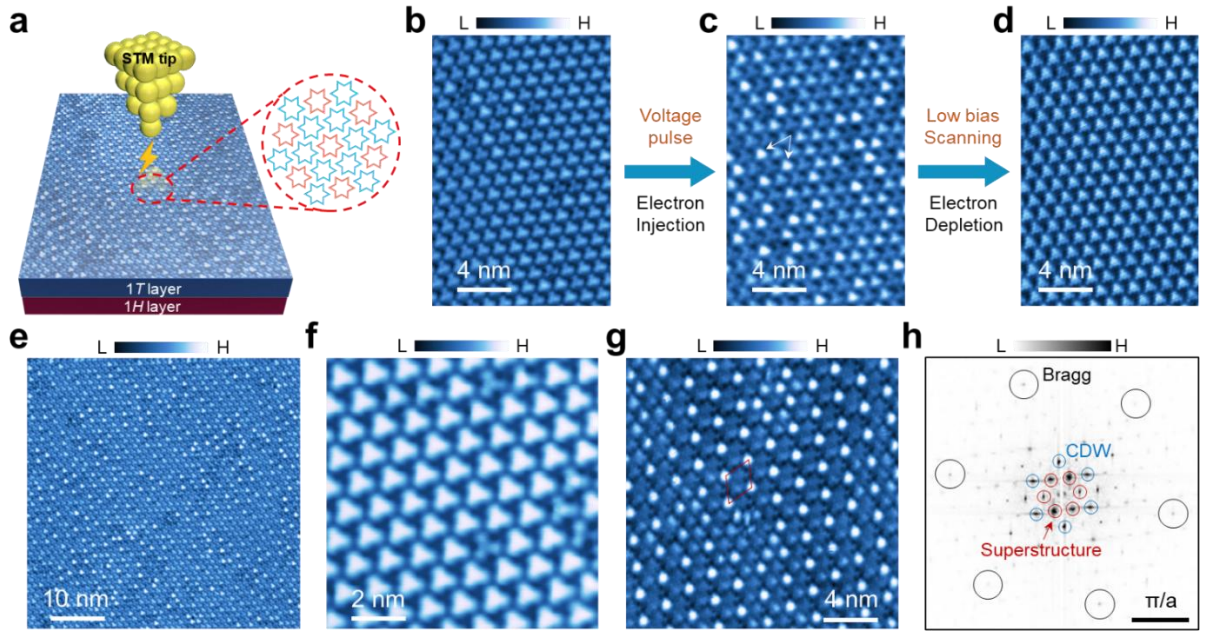


**Fig. 2 | Creation and depletion of electron-injected SoDs on the surface of 6R-TaS<sub>2</sub> 1T layer.** **a**, Schematic of the electron injection on the surface with STM voltage pulses. **b**, STM image of the 1T surface showing the periodic SoD lattice ( $V_s = -1000$  mV,  $I_t = 1$  nA). **c**, STM image of **b** after applying STM voltage pulses, showing creation of EI-SoDs ( $V_s = -1000$  mV,  $I_t = 1$  nA). **d**, STM image of **c** after continuous low-bias scanning, showing the depletion of the EI-SoDs ( $V_s = -1000$  mV,  $I_t = 1$  nA). **e**, Large-scale STM image of the mosaic superstructure ( $V_s = -500$  mV,  $I_t = 1$  nA), showing the coexistence of normal SoDs and EI-SoDs. **f,g**, Typical STM images in different regions of the voltage pulsed surface, showing the formation of ordered 1×1 (**f**) and  $\sqrt{3} \times \sqrt{3}$  (**g**) superstructures, respectively ( $V_s = -500$  mV,  $I_t = 1$  nA). **h**, FT image of **g**, showing both the CDW and  $\sqrt{3} \times \sqrt{3}$  superstructure on the EI-SoD surface.

To elucidate the nature of electron correlations in these phases, we performed spatially resolved scanning tunnelling spectroscopy (STS). In the 1×1 phase, a robust hard gap of ~330 meV is consistently observed (Fig. 3a-c), accompanied by well-defined lower and upper Hubbard bands (LHB and UHB) that closely resemble those of bulk 1T-TaS<sub>2</sub> crystal (Extended Data Fig. 4)<sup>32,33</sup>. These spectroscopic signatures indicate the emergence of a Mott insulating state, consistent with the localization of one electron on each depleted SoD cluster. Effectively, we utilized nanoscale manipulation to recover the pristine bulk 1T-TaS<sub>2</sub> Mott insulating state within the electron-depleted 1T layer in 6R-TaS<sub>2</sub>. In the  $\sqrt{3} \times \sqrt{3}$  superstructure, we observe qualitatively similar Hubbard-band features, although both the LHB and UHB are shifted slightly towards lower energies (Fig. 3d-f,

Extended Data Fig. 5). Notably, this insulating state develops at a fractional filling relative to the underlying SoD lattice, implying that Mott localization is stabilized not by integer filling of the original lattice but by interaction-driven charge ordering. This behaviour is consistent with a Wigner-Mott scenario, in which long-range Coulomb interactions induce an emergent superlattice that restores an odd-integer electron count per effective unit cell.

To verify the presence of charge ordering in the  $\sqrt{3}\times\sqrt{3}$  superstructure, which is the essential requirement of the Wigner-Mott insulating state, we perform detailed STM measurements. Similar superstructure is observed in transition-metal dichalcogenides via physical adsorption of alkali atoms<sup>34,35</sup>, chemical substitution<sup>36</sup> and chemical intercalation<sup>37</sup>. Importantly, this  $\sqrt{3}\times\sqrt{3}$  charge-ordered superstructure exhibits a pronounced contrast reversal under opposite bias polarities. The EI-SoD clusters appear as bright protrusions at a sample bias of -400 mV (Fig. 3g), whereas they become dim sites at 200 mV (Fig. 3h). This bias-dependent contrast reversal reflects a modulation of the local electronic density of states, confirming the electronic origin of the superstructure. Together with the observation of a robust Mott gap at fractional filling, these results provide compelling microscopic evidence that the  $\sqrt{3}\times\sqrt{3}$  phase realizes a Wigner-Mott insulating state.

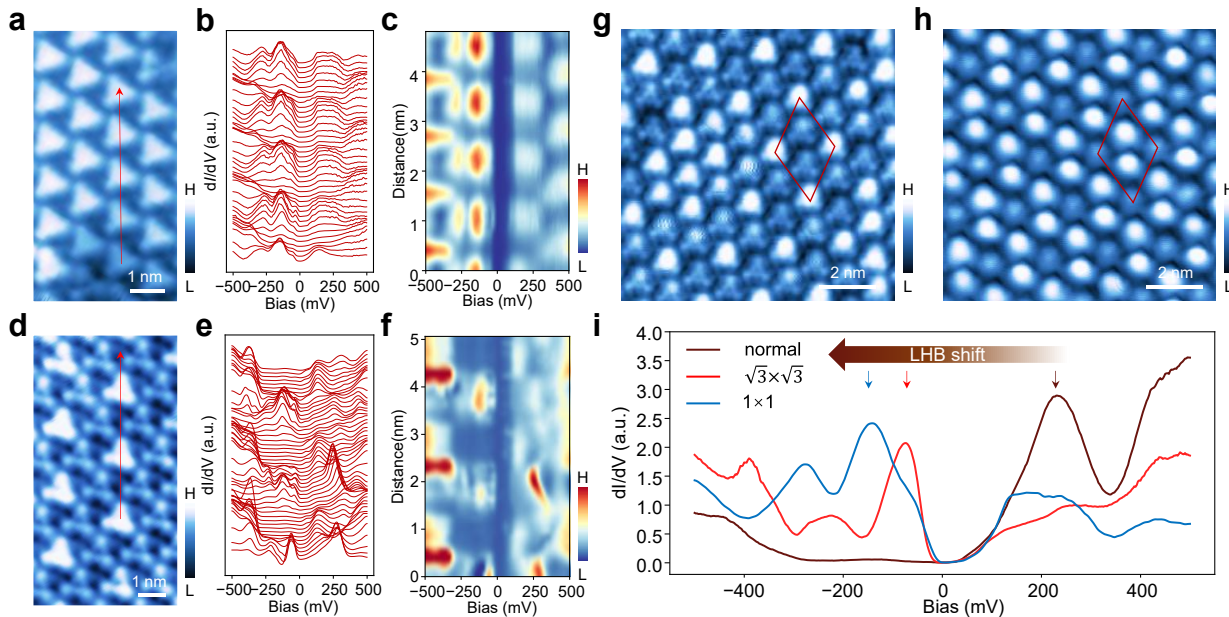


**Fig. 3 | STM/S of the Mott and Wigner-Mott insulating states in the ordered superstructures.** **a**, STM topography of a representative  $1\times 1$  superstructure ( $V_s = -500$  mV,  $I_t = 1$  nA). **b,c**, Waterfall plot and intensity map of the  $dI/dV$  spectra along the red arrow in **a**. **d**, STM topography of a representative  $\sqrt{3}\times\sqrt{3}$  superstructure ( $V_s = -500$  mV,  $I_t = 1$  nA). **e,f**, Waterfall plot and intensity map of the  $dI/dV$  spectra along the red arrow in **d**. **g,h**, STM images of the same area at -400 mV (**g**) and 200 mV (**h**), showing contrast reversal of the

$\sqrt{3} \times \sqrt{3}$  charge order ( $I_t=1$  nA). The red rhombuses mark the same unit cell of the superstructure at different bias voltages. **i**, Averaged  $dI/dV$  spectra taken at the centers of SoDs in the normal region (brown), and in the electron-injected SoDs of the  $\sqrt{3} \times \sqrt{3}$  (red) and  $1 \times 1$  (blue) superstructures.

We next compare the  $dI/dV$  spectra in different superstructures. In the original SoD lattice, the spectrum displays a pronounced peak at 230 mV, which is attributed to the lower Hubbard band (LHB)<sup>33,38,39</sup> in a hole-doped 2D Mott insulator. Upon electron doping from the tip, the LHB exhibits a gradual shift towards lower energies (Fig. 3i). In the  $\sqrt{3} \times \sqrt{3}$  and  $1 \times 1$  superstructures, the LHB at the EI-SoD shifts to -75 and -140 meV, respectively. This progressive shift of the LHB indicates an increasing electron doping level with greater electron injection. Notably, two important spectroscopic signatures emerge in the  $\sqrt{3} \times \sqrt{3}$  and  $1 \times 1$  superstructures. First, the LHB moves below the Fermi level, with the upper Hubbard band (UHB) appearing above it. Second, a hard gap of  $\sim 330$  meV develops between the LHB and UHB. Corresponding  $dI/dV$  linecut of mosaic region (Extended Data Fig 6) is also taken. Thus, STM tip induced electron doping generates a cascade of superstructure Mott insulating states. In the  $1 \times 1$  phase, strong correlations are dominated by the onsite Coulomb repulsion  $U$ , which enforces electron localization and drives the conventional Mott insulating behavior. By contrast, the  $\sqrt{3} \times \sqrt{3}$  insulating phase at one-third filling exhibits a spontaneously formed charge-ordered superlattice and a robust Mott gap, consistent with the defining characteristics of a Wigner-Mott insulating state in which both onsite interactions  $U$  and long-range Coulomb repulsion  $V$  play critical roles<sup>5,6,40</sup>.

Remarkably, we observe periodic ring states in the  $dI/dV$  maps of the  $\sqrt{3} \times \sqrt{3}$  superstructure. Under positive bias voltages, the rings form an ordered triangular lattice, each centered on an EI-SoD (Fig. 4a,b). Under negative bias voltages, the same region instead exhibits a honeycomb lattice of rings centered on the remaining SoDs (Fig. 4c). The ring diameters display spatial variation and increase linearly with bias magnitude for both polarities (Fig. 4d-i, Extended Data Figs. 7 and 8). Such ring states have been theoretically predicted in topological and Mott insulators<sup>41,42</sup>, where local potentials induced by defects create bound states through doublon-holon coupling. In STM measurements, the tip acts as a local top gate, producing band bending that facilitates tunneling-induced doublon (positive bias) and holon (negative bias) excitations.

A classical interpretation of these ring-like features invokes a tip-induced charging and discharging process<sup>43,44</sup>. When the STM tip is positioned above an EI-SoD in the  $\sqrt{3}\times\sqrt{3}$  superstructure, the injected electron can be discharged under positive sample bias due to the strong electric field between the tip and the substrate. As the tip moves away, the electron can subsequently refill the SoD. Such discharge events typically produce ring-like features in  $dI/dV$  maps, accompanied by sharp spikes in the local  $dI/dV$  spectra<sup>45,46</sup>. Similarly, charging of initially unoccupied SoD clusters from the EI-SoD clusters gives rise to analogous ring features at negative sample bias. Consistent with this picture, hexagonally packed rings are observed at the bright EI-SoD sites under positive bias, whereas honeycomb-packed rings emerge around the dark, unoccupied SoDs at negative bias. Moreover,  $dI/dV$  line cuts taken across these rings resolve two sets of sharp spectral spikes at positive and negative bias voltages, respectively (Extended Data Fig. 9).

Notably, the ring-like features emerge exclusively in the  $\sqrt{3}\times\sqrt{3}$  superstructure. To establish their intimate connection to the superstructure Mott insulating state, we deliberately identify a boundary between the normal region and the  $\sqrt{3}\times\sqrt{3}$  phase (Extended Data Fig. 10a). While the lower-right region exhibits the original depleted SoD lattice, the upper-left region hosts the  $\sqrt{3}\times\sqrt{3}$  charge-ordered superstructure. Correspondingly, the  $dI/dV$  maps reveal that the ring features are strictly confined to the  $\sqrt{3}\times\sqrt{3}$  region and are entirely absent in the normal depleted SoD region (Extended Data Fig. 10b, c), demonstrating that these states are intrinsic to the superstructure phase.

Consistent with this observation, no ring features are detected in either the  $1\times 1$  Mott phase or the bulk  $1T$ -TaS<sub>2</sub> crystal (Extended Data Figs. 11 and 12). This exclusion rules out charge exchange between the EI-SoDs and the underlying  $1H$  layer within the experimental energy window. In the  $\sqrt{3}\times\sqrt{3}$  phase, injected electrons can only be transiently discharged from EI-SoD sites into neighboring, initially depleted SoDs permitted by the superlattice. The selective emergence of ring features therefore reflects enhanced inter-site Coulomb interactions within the  $\sqrt{3}\times\sqrt{3}$  superlattice, a behavior naturally captured by a Wigner-Mott framework (Extended Data Fig. 13).

To further elucidate the roles of onsite ( $U$ ) and inter-site ( $V$ ) interactions in the  $\sqrt{3}\times\sqrt{3}$  phase, we perform repeated STM scans at bias voltages exceeding the charging/discharging threshold. Although electrons can be transiently displaced from the EI-SoD sites during scanning, we find that, once the tip is removed, they spontaneously relax back to their original sites, while the  $\sqrt{3}\times\sqrt{3}$  charge-ordered pattern remains intact over repeated topographic and spectroscopic measurements (Fig. 4d-i, Extended Data Fig. 14). This reversible relaxation behavior indicates that the  $\sqrt{3}\times\sqrt{3}$  charge-ordered lattice

constitutes a stable energy minimum and is resilient against local electrostatic perturbations. Such self-restoring dynamics directly reflect the presence of strong inter-site Coulomb interactions, which actively stabilize the charge order and underscore the essential role of  $V$  in the Wigner-Mott insulating state.

Taken together, our results establish a real-space realization of a Wigner-Mott insulating state, in which Mott localization and interaction-driven charge ordering coexist and mutually reinforce each other (Fig. 4j). In contrast to conventional Mott insulators governed predominantly by onsite  $U$ , and to Wigner crystals stabilized solely by long-range  $V$ , the  $\sqrt{3}\times\sqrt{3}$  phase in 6R-TaS<sub>2</sub> exhibits a robust Hubbard gap persists at fractional filling, and a spontaneous charge-ordered superlattice emerging from inter-site Coulomb interactions. Crucially, the charge-ordered pattern is not only statically resolved but also dynamically stabilized, as evidenced by the reversible recovery of the superlattice following repeated tip-induced charging and discharging events. This self-restoring behavior demonstrates that the  $\sqrt{3}\times\sqrt{3}$  charge-ordered lattice represents a global energy minimum protected by long-range Coulomb interactions and is robust against external perturbations. These results thus provide direct microscopic evidence for the cooperative roles of  $U$  and  $V$  in stabilizing a Wigner-Mott insulator (Fig. 4j).

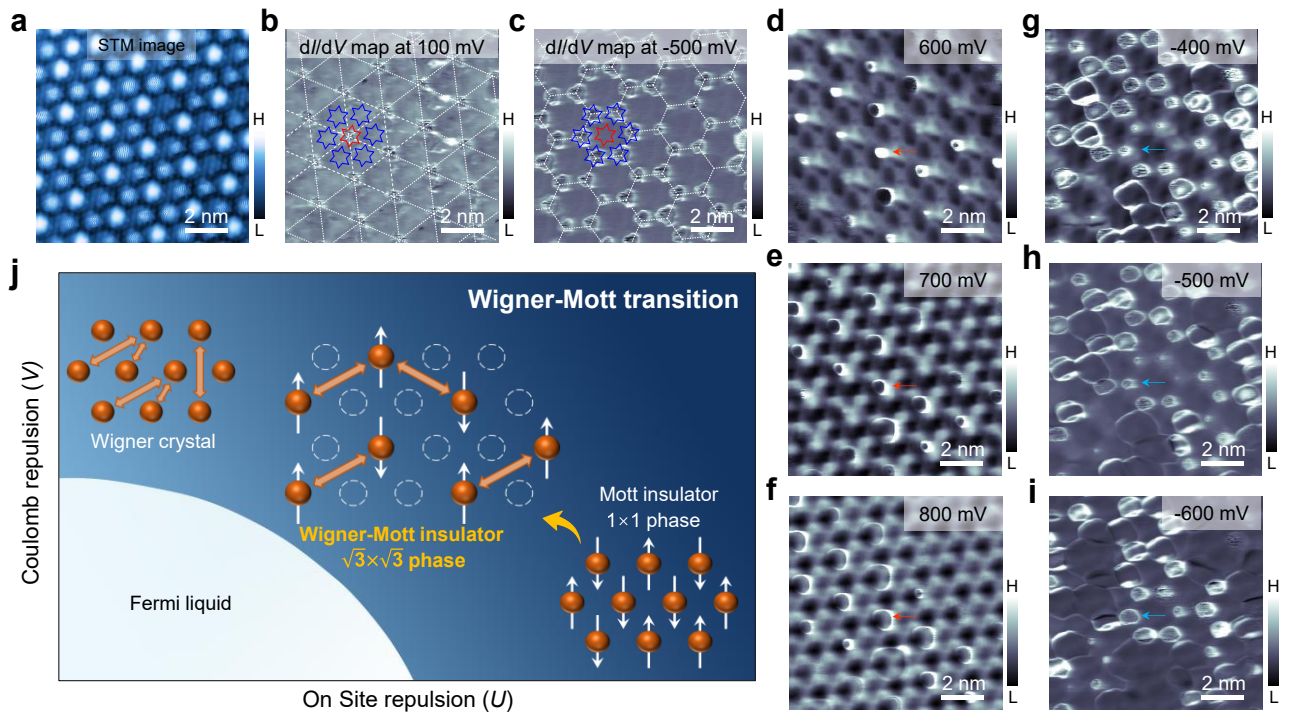


**Fig. 4 | STM/S of the  $\sqrt{3}\times\sqrt{3}$  Wigner-Mott insulating phase on the 1T surface.** **a**, STM topography of a representative  $\sqrt{3}\times\sqrt{3}$  superstructure ( $V_s = -500$  mV,  $I_t = 1$  nA). **b**, dI/dV map of the region in **a** at 100 mV, showing the formation of triangular lattice of rings centered at the electron-injected SoDs (red). **c**, dI/dV map

of the region in **a** at -500 mV, showing formation of honeycomb lattice of rings centered at the remaining SoDs (blue). **d-f**,  $dI/dV$  maps of a  $\sqrt{3} \times \sqrt{3}$  superstructure at 600, 700 and 800 mV, respectively, showing spatial dispersion of the discharging rings. **g-i**,  $dI/dV$  maps of a  $\sqrt{3} \times \sqrt{3}$  superstructure at -400, -500 and -600 mV, respectively, showing similar spatial dispersion of the charging rings. **j**, Phase diagram of Wigner-Mott transition.

In summary, we have realized and directly visualized a Wigner-Mott insulating state on the  $1T$ -terminated surface of  $6R$ -TaS<sub>2</sub>. We achieve microscopic control of electron filling and uncover a  $\sqrt{3} \times \sqrt{3}$  insulating phase characterized by a spontaneously formed charge-ordered superlattice and a robust Mott gap at fractional filling. The coexistence of real-space charge order and genuine Mott localization provides direct evidence for a Wigner-Mott insulating state, in which both onsite Coulomb repulsion  $U$  and inter-site interaction  $V$  play essential roles. Our results establish  $6R$ -TaS<sub>2</sub> as a unique platform for the real-space investigation of Wigner-Mott physics and pave the way for controlled studies of correlation-driven electronic phases beyond conventional Mott paradigms.

## References

1. Camjayi, A., Haule, K., Dobrosavljevic, V. & Kotliar, G. Coulomb correlations and the Wigner-Mott transition. *Nat. Phys.* **4**, 932 (2008).
2. Li, C. H. & Wang, Z. Q. Mott and Wigner-Mott transitions in doped correlated electron systems: Effects of superlattice potential and intersite correlation. *Phys. Rev. B* **80**, 125130 (2009).
3. Regan, E. C. et al. Mott and generalized Wigner crystal states in WSe<sub>2</sub>/WS<sub>2</sub> moire superlattices. *Nature* **579**, 359 (2020).
4. Li, H. Y. et al. Imaging two-dimensional generalized Wigner crystals. *Nature* **597**, 650 (2021).
5. Tang, Y. H. et al. Dielectric catastrophe at the Wigner-Mott transition in a moire superlattice. *Nat. Commun.* **13**, 4271 (2022).
6. Tang, Y. H. et al. Evidence of frustrated magnetic interactions in a Wigner-Mott insulator. *Nat. Nanotechnol.* **18**, 233 (2023).
7. Mott, N. F. The Basis of the Electron Theory of Metals, with Special Reference to the Transition Metals. *Proc. Phys. Soc. A* **62**, 416 (1949).
8. Keimer, B. et al. From quantum matter to high-temperature superconductivity in copper oxides. *Nature* **518**, 179 (2015).
9. Lee, P. A., Nagaosa, N. & Wen, X. G. Doping a Mott insulator: Physics of high-temperature superconductivity. *Rev. Mod. Phys.* **78**, 17 (2006).
10. Sipos, B. et al. From Mott state to superconductivity in 1T-TaS<sub>2</sub>. *Nat. Mater.* **7**, 960 (2008).
11. Tranquada, J. M. et al. Evidence for Stripe Correlations of Spins and Holes in Copper-Oxide Superconductors. *Nature* **375**, 561 (1995).
12. Lake, B. et al. Antiferromagnetic order induced by an applied magnetic field in a high-temperature superconductor. *Nature* **415**, 299 (2002).
13. Legros, A. et al. Universal T-linear resistivity and Planckian dissipation in overdoped cuprates. *Nat. Phys.* **15**, 142 (2019).
14. Cooper, R. A. et al. Anomalous Criticality in the Electrical Resistivity of La<sub>2-x</sub>Sr<sub>x</sub>CuO<sub>4</sub>. *Science* **323**, 603 (2009).
15. Qiu, Z. Z. et al. Evidence for electron-hole crystals in a Mott insulator. *Nat. Mater.* **23**, 1055 (2024).

16. Achari, A. et al. Alternating Superconducting and Charge Density Wave Monolayers within Bulk 6R-TaS<sub>2</sub>. *Nano Lett.* **22**, 6268 (2022).
17. Liu, S. B. et al. Nematic Ising superconductivity with hidden magnetism in few-layer 6R-TaS<sub>2</sub>. *Nat. Commun.* **15**, 7569 (2024).
18. Thompson, A. H. The synthesis and properties of 6R-TaS<sub>2</sub>. *Solid State Commun.* **17**, 1115 (1975).
19. Wang, S. P. et al. Pressure Induced Nonmonotonic Evolution of Superconductivity in 6R-TaS<sub>2</sub> with a Natural Bulk Van der Waals Heterostructure. *Phys. Rev. Lett.* **133**, 056001 (2024).
20. Yan, L. M. et al. Double Superconducting Dome of Quasi Two-Dimensional TaS<sub>2</sub> in Non-Centrosymmetric van der Waals Heterostructure. *Nano Lett.* **24**, 6002 (2024).
21. Crippa, L. et al. Heavy fermions vs doped Mott physics in heterogeneous Ta-dichalcogenide bilayers. *Nat. Commun.* **15**, 1357 (2024).
22. Vano, V. et al. Artificial heavy fermions in a van der Waals heterostructure. *Nature* **599**, 582 (2021).
23. Li, M. et al. Ordered and tunable Majorana-zero-mode lattice in naturally strained LiFeAs. *Nature* **606**, 890 (2022).
24. Nayak, A. K. et al. Evidence of topological boundary modes with topological nodal-point superconductivity. *Nat. Phys.* **17**, 1413 (2021).
25. Nayak, A. K. et al. First-order quantum phase transition in the hybrid metal-Mott insulator transition metal dichalcogenide 4Hb-TaS. *P. Natl. Acad. Sci. Usa.* **120**, e2304274120 (2023).
26. Sánchez-Ramírez, I., Vergniory, M. G. & de Juan, F. Charge transfer in heterostructures of T and H transition metal dichalcogenides. *Phys. Rev. B* **110**, 195138 (2024).
27. Ayani, C. G. et al. Unveiling the Interlayer Interaction in a 1H/1T TaS<sub>2</sub> van der Waals Heterostructure. *Nano Lett.* **24**, 10805 (2024).
28. Huang, X. et al. Doped Mott Phase and Charge Correlations in Monolayer 1T-NbSe<sub>2</sub>. *Phys. Rev. Lett.* **134**, 046504 (2025).
29. Ribak, A. et al. Chiral superconductivity in the alternate stacking compound 4Hb-TaS<sub>2</sub>. *Sci. Adv.* **6**, eaax9480 (2020).
30. Mao, J. H. et al. Realization of a tunable artificial atom at a supercritically charged vacancy in graphene. *Nat. Phys.* **12**, 545 (2016).

31. Tan, Y., Tsang, P. K. H., Dobrosavljević, V. & Rademaker, L. Doping a Wigner-Mott insulator: Exotic charge orders in transition metal dichalcogenide moiré heterobilayers. *Phys. Rev. Research* **5**, 043190 (2023).
32. Butler, C. J., Yoshida, M., Hanaguri, T. & Iwasa, Y. Mottness versus unit-cell doubling as the driver of the insulating state in 1T-TaS<sub>2</sub>. *Nat. Commun.* **11**, 2477 (2020).
33. Butler, C. J., Yoshida, M., Hanaguri, T. & Iwasa, Y. Doublonlike Excitations and Their Phononic Coupling in a Mott Charge-Density-Wave System. *Physical Review X* **11**, 011059 (2021).
34. Lee, J. et al. Honeycomb-Lattice Mott Insulator on Tantalum Disulphide. *Phys. Rev. Lett.* **125**, 096403 (2020).
35. Bang, J. et al. Charge-ordered phases in the hole-doped triangular Mott insulator 4Hb-TaS<sub>2</sub>. *Phys. Rev. B* **109**, 195170 (2024).
36. Geng, Y. Y. et al. Correlated electrons in the flat band in the charge density wave state of 4Hb-TaSexS<sub>2-x</sub>. *Phys. Rev. B* **110**, 115107 (2024).
37. Shen, S. W. et al. Inducing and tuning Kondo screening in a narrow-electronic-band system. *Nat. Commun.* **13**, 2156 (2022).
38. Cho, D. et al. Nanoscale manipulation of the Mott insulating state coupled to charge order in 1T-TaS<sub>2</sub>. *Nat. Commun.* **7**, 10453 (2016).
39. Chen, Y. et al. Evidence for a spinon Kondo effect in cobalt atoms on single-layer 1T-TaSe<sub>2</sub>. *Nat. Phys.* **18**, 1335 (2022).
40. Hubbard, J. Generalized Wigner Lattices in One Dimension and Some Applications to Tetracyanoquinodimethane (Tcnq) Salts. *Phys. Rev. B* **17**, 494 (1978).
41. Queiroz, R. et al. Ring states in topological materials. *arXiv:2406.03529* 2024 (2024).
42. Pangburn, E., Banerjee, A., Pépin, C. & Bena, C. Impurity-induced Mott ring states and Mott zeros ring states in the Hubbard operator formalism. *Phys. Rev. B* **112**, 125157 (2025).
43. Marczinowski, F. et al. Effect of charge manipulation on scanning tunneling spectra of single Mn acceptors in InAs. *Phys. Rev. B* **77**, 115318 (2008).
44. Li, H. Y. et al. Imaging local discharge cascades for correlated electrons in WS<sub>2</sub>/WSe<sub>2</sub> moiré superlattices. *Nat. Phys.* **17**, 1114 (2021).
45. Li, H. Y. et al. Mapping charge excitations in generalized Wigner crystals. *Nat. Nanotechnol.*

**19**, 618 (2024).

46. Li, C. et al. Strong signature of electron-vibration coupling in molecules on Ag(111) triggered by tip-gated discharging. *Nat. Commun.* **14**, 5956 (2023).

## Methods

### Single-crystal growth

The 6R-TaS<sub>2</sub> single crystals were grown using Chemical Vapor Transport techniques, with NH<sub>4</sub>Cl as the transport agent. A stoichiometric amount of high-purity tantalum powder (Ta, 99.99%) and sulfur lumps, along with 50 mg of ammonium chloride (NH<sub>4</sub>Cl), were placed in a silica ampule and sealed under vacuum (10<sup>-3</sup> Torr). The ampule was then placed in a two-zone horizontal furnace, with the source end positioned in the hot zone and the growth end in the cold zone. The furnace was maintained at constant temperatures of 1050°C and 950°C for 150 hours. After the growth, the system was allowed to cool naturally to room temperature. High-quality 6R-TaS<sub>2</sub> single crystals were obtained from the cold end of the ampule.

### STM/S experiments

A 6R-TaS<sub>2</sub> crystal was mounted onto a STM sample holder in a glove box and then transferred to an ultra-high vacuum chamber. The crystal was cleaved *in-situ* at a temperature of 80 K. After cleavage, the sample was immediately transferred to the STM scanner. The STM/S measurements were conducted in an ultra-low temperature STM system. Tungsten tips were etched chemically and calibrated on Au(111) surfaces before use. The dI/dV spectra and maps were obtained using a standard lock-in technique with a modulation voltage of 5 mV at 973.0 Hz. All the images, spectra and dI/dV maps were taken at 40 mK.

**Acknowledgements:** The work is supported by the National Key Research and Development Projects of China (2024YFA1207700, 2022YFA1204100), National Natural Science Foundation of China (62488201), the CAS Project for Young Scientists in Basic Research (YSBR-003), the Youth Innovation Promotion Association (2023005), and the Quantum Science and Technology-National Science and Technology Major Project (2021ZD0302700). Z.W. is supported by the US DOE, Basic Energy Sciences Grant No. DE-FG02-99ER45747 and by Research Corporation for Science Advancement Cottrell SEED Award No. 27856.

**Author Contributions:** H.-J.G. supervised the project. H.-J.G. and G.L. designed the experiments. K.Z. and H.Y. prepared samples. H.X., G.L., Y.H. and Y.Y. performed STM experiments with guidance of H.-J.G. and Z.W. provided theoretical consideration. G.L., H.X., Z.W. and H.-J.G. analysed the data and wrote the manuscript. All of the authors participated in analysing experimental data, plotting figures, and writing the manuscript.

**Data availability:** Data measured or analysed during this study are available from the corresponding author on reasonable request. Source data are provided with this paper.

**Competing Interests:** The authors declare that they have no competing interests.